International Journal of Hydrogen Energy 228 (2026) 154628

Contents lists available at ScienceDirect

International Journal of Hydrogen Energy

journal homepage: www.elsevier.com/locate/he

In-situ investigation of corrosion resistance of Au-coated bipolar plates for SO_2 depolarized electrolysis

Sakeb Choudhury [a,*], Dimitrios Dimitrakis [a], Dennis Thomey [a], Timo Ott [b], Céline Réthoré [b], Jonas Michels [b], Martin Kürten [b]

[a] German Aerospace Centre, Institute of Future Fuels, Im Langenbroich 13, Jülich, 52428, Germany
[b] GRILLO Chemicals GmbH, Weseler Straße 1, 47169, Duisburg, Germany

ARTICLE INFO

Keywords:
Westinghouse cycle
SO_2 depolarized electrolysis
Bipolar plate corrosion
Corrosion resistance
Corrosion rate
Au-coating

ABSTRACT

In Sulphur dioxide Depolarized Electrolysis (SDE), Au-coatings can serve as protective layers for bipolar plates and play a critical role for SDE efficiency. Despite its importance, there is a notable gap in literature regarding the electrochemical stability of Au-films and their ability to protect the bipolar plates against electrochemical corrosion. In this report, an experimental setup is employed to monitor and quantitatively assess the electrochemical corrosion of Au-coated bipolar plates under SDE-relevant conditions. The corrosion resistance of cathode arc assisted PVD and electron beam evaporated Au-coating on three different bipolar plate materials: Graphite, Hastelloy, and 904L Stainless Steel was evaluated by implementing an Accelerated Corrosion Test (ACT) combined with *in-situ* elemental analysis. The results show that cathodic arc PVD Au-films and Graphite bipolar plate demonstrates the highest corrosion resistance. The ability of cathode arc PVD Au-coating to homogenously coat different bipolar plate materials further highlights its suitability for SDE operation.

1. Introduction

Electrolysis of water occupies the current centre stage for efficient and emission free, green H_2 production. Proton Exchange Membrane Electrolysis (PEMEL), Alkaline Electrolysis (AEL) and Solid Oxide Electrolyzer cell (SOEC) are the frontrunners and have created a rapidly growing, transformative market for green hydrogen. These technologies are envisioned as the forefront of sustainable hydrogen production and are often viewed as key enablers for a clean energy transition. However, bottlenecks lie in high-power consumption, use of expensive or critical materials and various technical aspects [1–3]. Among them, SOEC requires the lowest specific electricity consumption 40-42 kWh kg^{-1} H_2, offers high efficiency and potential integration with industrial waste heat. However, their long start-up times to reach operating temperature (800-1000°C) and thermal cycling degrades materials and lifetime. Compared to SOEC, PEMEL is capable of operating at low temperature to produce high purity H_2 at high current densities ($\leq$2000 mA cm^{-2}). The typical process consumption lies within the range of 52-58 kWh kg^{-1} H_2 at large scale. Nevertheless, they rely on critical raw materials (CRM) such as scarce noble metals (Ir, Pt) and toxic non-biodegradable PFAS polymer membranes. AEL show comparable electricity demand (53–56 kWh kg^{-1} H_2) while implementing non-CRM catalysts; however, this technology is yet to be matured and suffers from numerous technical issues such as membrane stability and durability. An interesting alternative, with significantly lower power consumption and the promise of critical material free operation is the SO_2 Depolarized Electrolysis (SDE) [4]. It was first developed in the 70s as part of the Westinghouse cycle – or Hybrid Sulphur (HyS) cycle, where it is supported by a (solar) thermochemical process. The thermochemical cycle can be powered by a renewable energy source such as Concentrated Solar Technologies (CST) to split H_2SO_4 into SO_2, O_2 and H_2O [5,6]. The produced SO_2 is fed to the SDE to electrochemically convert it into H_2SO_4 -thus closing the cycle, while simultaneously producing high-purity H_2. Consequently, SDE can be a prime candidate for a viable technology for large-scale, carbon-free H_2 generation. At the same time SDE is of interest, not only as part of the HyS cycle but also as a stand-alone technology for H_2 production whenever a source of SO_2 is available, as is the case in the sulphuric acid industry.

A typical two-electrode SDE cell is shown in Fig. 1 where the proton exchange membrane is positioned at the centre with the unipolar plates

* Corresponding author.
E-mail addresses: sakeb.choudhury@dlr.de (S. Choudhury), dimitrios.dimitrakis@dlr.de (D. Dimitrakis), dennis.thomey@dlr.de (D. Thomey), t.ott@grillo.de (T. Ott), c.rethore@chemad.de (C. Réthoré), j.michels@grillo.de (J. Michels), m.kuerten@grillo.de (M. Kürten).

https://doi.org/10.1016/j.ijhydene.2026.154628
Received 20 November 2025; Received in revised form 10 March 2026; Accepted 18 March 2026
Available online 24 March 2026

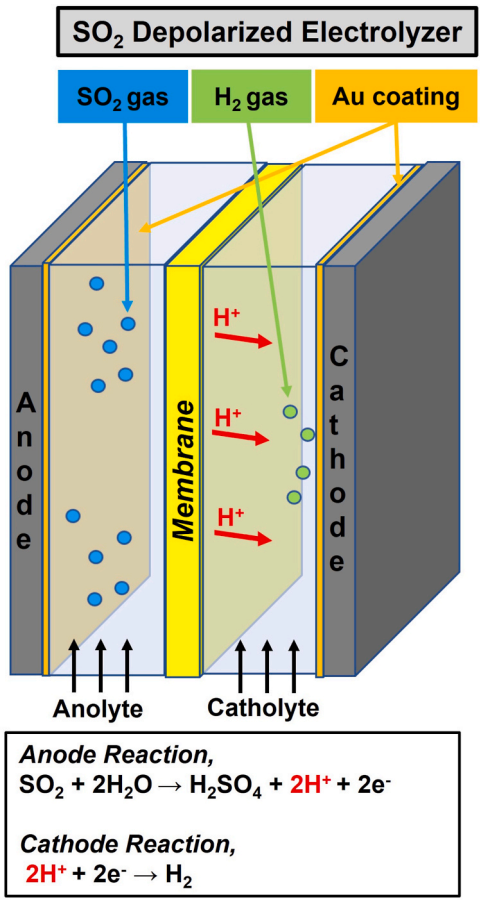

Fig. 1. Typical cell setup of a SO_2 depolarized electrolyser: SO_2 (blue spheres) dissolved in the anolyte is electrochemically oxidized to H_2SO_4, the protons permeate through the membrane to reach the cathode and are reduced to H_2 gas (green spheres). Au-coating on the plates works as a corrosion protective layer. (For interpretation of the references to colour in this figure legend, the reader is referred to the Web version of this article.)

at the sides (or bipolar plates for multiple/stacked cells). During the operation of the SDE cell, the SO_2 molecules in the anolyte are electrocatalytically converted into H_2SO_4 while the Hydrogen Evolution Reaction (HER) takes place at the cathode side. The theoretical standard potential of the overall reaction (Eq. (1)) indicates a significantly lower energy requirement compared to conventional water electrolysis (E° = 1.23 V) [5,7]. [8].

$$SO_2 + 2H_2O = H_2SO_4 + H_2 \ (E^\circ = \sim 0.16 \text{ V at } 298 \text{ K}, 1 \text{ atm}) \qquad \text{Eq. 1}$$

One of the challenges of SDE operation, is the electrochemical corrosion of components of the cell/stack such as the bipolar plates. There are literature sources available, documenting corrosion resistance of various materials with respect to H_2SO_4 concentration and temperature [9,10]. However, their testing conditions do not include any applied potential. Hence these references do not reflect corrosion resistance correlating to the operating conditions of the SDE. In literature, the common operating parameters of SDE ranges from <1 to <1.7 V with a typical anolyte/catholyte H_2SO_4 concentration of 10-40 wt% [11–13]. Under such conditions, corrosion mechanisms and rates differ markedly compared to the available iso-corrosion diagrams [9,10]. Therefore, an experimental and quantitative methodology needs to be devised in order to systematically evaluate corrosion resistance of Au-coated bipolar plates under relevant conditions.

Graphite is always regarded as a very good candidate as it is stable at high potential applications and is widely used for lab-scale water splitting experiments [14,15]. However, it incurs higher processing cost, processing dependent conductivity profiles and lacks mechanical strength. So, Stainless steel is often preferred in terms of realistic scaled-up SDE operations [16]. Preliminary literature survey indicated that the 904L Stainless Steel shows low corrosion rate in H_2SO_4 environments and is capable of withstanding corrosion against 30 wt% H_2SO_4 compared to 316L Stainless Steel [8], attributed to the Mo-content of the former. Similarly, another Mo-containing Ni-based alloy, Hastelloy-C276 was included as the third choice of bipolar plate material in this work. Hastelloy is well known for its superior corrosion resistance and ability to perform in extreme conditions. To date, the systematic study of corrosion resistance of 904L Stainless Steel and Hastelloy under conditions relevant to SDE operation is still missing in literature.

1.1. Objective and experimental methodology

From Fig. 1, it can be understood that Au-coatings serve as both catalyst and protective layer for both electrodes and constitute a major cost factor in SDE. Their durability and electrochemical performance are crucial for SDE system efficiency. Despite this signficance, the extent to which Au films can stabilize and shield current collectors from corrosion in SDE environments remains unclear. The only reported state-of-the-art Au-layer deposition method for the SDE bipolar plates is arc-assisted Physical Vapor Deposition (PVD) [11]. The Au-film deposition method must ensure a high-quality Au-film to exhibit uniformity, high corrosion resistance and durability to withstand longtime SDE operation. A strong adhesion between the bipolar plate material and the Au-coating is also necessary to prevent any Au-coating delamination during operation. Within the published research of SDE material development, no literature could be identified where both corrosive H_2SO_4 electrolyte and simultaneous electrochemical potential was implemented on different bipolar plate materials and Au-coatings for a side-by-side comparison of their corrosion resistance. Most publications report performance characterization, catalyst evaluation, and long-term voltage trends for SDE. Some papers considered common bipolar plate materials and arc assisted PVD Au-coatings [8,11], but with a significantly different electrochemical testing protocol compared to SDE operation. Overall, the scientific inquiry about the electrochemical stability of different Au-coating methods as well as the different bipolar plate materials is still to be investigated in a detail manner. The main objective of this paper is to bridge this knowledge gap by demonstrating an *in-situ* experimental framework to study the electrochemical corrosion of different Au-coated bipolar plate materials within the SDE operating conditions.

The electrochemical corrosion study in this work, is conducted with a combination of two simultaneous measurements; first, an electrochemical measurement protocol termed “Accelerated Corrosion Test” (ACT) to introduce electrochemical corrosion to both uncoated and Au-coated bipolar plate coupons using ascending potential steps with varied durations, representative of SDE operating conditions. Secondly, a simultaneous *in-situ* elemental analysis of the electrolyte using Inductively Coupled Plasma Optical Emission Spectroscopy (ICP-OES) to detect and quantify corrosion products originating from the coupons. Altogether, the experimental methodology allows a clear visual monitoring of electrochemical corrosion as well as real-time synchronous sampling of liquid electrolyte specimen during an ongoing electrochemical experiment. As the ACT progresses, corrosion byproducts detach from the coupon surface and diffuse into the electrolyte, hence the *in-situ* ICP-OES elemental analysis enables a direct quantitative correlation between applied potential and material degradation. The elemental concentration from ICP-OES data constitutes the first electrochemical corrosion metric (Metric 1). Further on, electrochemical measurements are performed to calculate the Corrosion Rate (CR) of the coupons before and after ACT. The CR shift with respect to the ACT convey the second electrochemical corrosion metric (Metric 2). These two metrics serve as quantitative indicators to identify the most effective Au-coating method and optimal bipolar plate material for the SDE

application. Scanning Electron Microscopy (SEM) is employed to observe morphological changes of the coupons, while Energy Dispersive X-ray Spectroscopy (EDX) is utilized for the compositional analysis across different coupons.

2. Materials and methods

2.1. Bipolar plate materials and Au-coating methods

A series of Au-coated coupons was prepared using two different PVD techniques: Electron beam (E-beam) evaporation and Cathodic Arc-assisted PVD (CA). Three substrate materials were selected for Au-coating; Graphite (G), Hastelloy (HA), and 904L stainless steel (904L). Starting from a bipolar plate of a SDE cell, coupons of each bipolar plate material were cut with dimensions of 20 x 19 mm. Throughout this study, the coupon name is organized as substrate_coating-method_coupon-no and all uncoated reference coupons (G_0_2, HA_0_1, and 904L_0_1) are included for baseline comparison. For E-beam evaporated coupons (G_Ebeam_1, HA_Ebeam_1, 904L_Ebeam_1), all three substrates were coated with a 10 nm Titanium (Ti) adhesion layer followed by a 150 nm Au-layer via E-beam evaporation. E-beam evaporation was performed in a vacuum chamber with a base pressure of 5×10^{-6} mbar. During the E-beam evaporation, all three coupons were kept at room temperature and were coated simultaneously from an Au target of 99.99% purity with 2-5 nm Au granulates. For Cathode Arc-assisted PVD coupons (G_CA_1, HA_CA_1, 904L_CA_1), a 100 nm Ti-adhesion layer and a 100 nm Au-coating were applied on top of all three substrates at the same time as previously done in literature [17] for a thermoelectric application. The CA deposition was performed in vacuum with base/working pressure of $\sim 10^{-5}$ mbar without any carrier gas from a target with purity of 99.99% while keeping the substrates at room temperature. For maintaining the same film thickness of Ti and Au on all three coupons, they were coated in the CA PVD deposition step at the same time.

2.2. Experimental setup

Electrochemical corrosion experiments were performed with an "AMTEK K0235 Electrochemical Flat Cell", selected for its three-electrode setup, ease of manipulation during electrolyte sample collection for ICP-OES and will be referred to as corrosion cell or simply cell in this work. Details of the cell, coupon loading/unloading procedure and electrolyte sampling process are discussed in section 1 of the supporting information. All experiments were performed in room temperature and ambient pressure to isolate the influence of corrosion potential on the Au-coated coupons with different bipolar plate materials. Although SDE systems typically operate at 80-120°C, the objective of this study is to achieve a comparative evaluation of different coating–substrate combinations. While elevated temperatures may influence absolute corrosion rates, the relative corrosion trends between materials are expected to remain comparable, enabling a meaningful assessment of coating performance. The electrolyte was chosen to be 20 wt% H_2SO_4 and was kept stationary without any stirring or purging. The coupon size was kept constant (20 mm × 19 mm) and the exposed area of the coupon to the electrolyte had a diameter of 10 mm. The potential is expressed in the Reverse Hydrogen Scale (RHE) which is converted from the reference electrode Ag/AgCl.

2.3. Accelerated corrosion test

To perform the accelerated corrosion test, a Linear Sweep Voltammetry (LSV) with a scan rate of 50 mV/s from the Open Circuit Potential (OCP) to 1.2 V is conducted first, followed by a Chronoamperometric potential of 1.2 V for 2 h. This is considered the first potential step (Step 1) of the ACT. Towards the end of Step 1 completion, an electrolyte sample is collected, and a second LSV is performed starting from 1.2 V (50 mV/s), reaching the potential of 1.5 V (Step 2) and the potential 1.5 V is maintained for 30 min. Similarly, a 3rd LSV is employed to raise the potential from 1.5 V to 1.7 V (Step 3) at the end of Step 2. Since 1.7 V is a high anodic potential, the duration of Step 3 is limited to 10 min.

2.4. I_{corr} measurement (corrosion rate)

I_{corr} measurement is a LSV measurement, performed from the cathodic side, with a window of 500 mV (−250 mV to +250 mV) with respect to the OCP and with a very slow scan rate 0.125 mV/s. Special care is taken before starting the I_{corr} measurement where sufficient time is given for the OCP to stabilize in the fresh electrolyte. From the I_{corr} measurement, the mass loss rate and Corrosion rate are calculated.

2.5. In-situ elemental analysis

In-situ elemental analysis of the collected electrolyte samples is performed using the SPECTRO ICP-OES ARCOS with model FHX3X (Au-) and FMX46 (Fe-, Ni-, Cr-). This particular analytical method can trace metals down to parts-per-million (ppm) levels in liquid phase. For the investigation of this experimental work, the ICP-OES analysis is focused on concentrations of Au-, Fe-, Ni- and Cr- in electrolyte samples.

2.6. Scanning Electron Microscopy and Energy Dispersive X-ray

Scanning Electron Microscopy (SEM) is a key technique for analysing surface morphology by providing detailed information about the surface roughness, defect and texture. SEM imaging was performed using a Zeiss Ultra 55 Microscope. Images were taken with magnification ranging from 35 to 20,000x. A SEM integrated Energy Dispersive X-ray (EDX) system is utilized for a spatially resolved compositional analysis. The EDX measurements examine the change of elemental composition between the electrochemically exposed surface area and the peripheral unexposed surface area with the assistance of the adjustable probing depth. The dataset contained EDX derived cumulative elemental analysis from three different spots (50 μm × 50 μm) inside both electrochemical exposed and unexposed areas. This enables the statistical composition analysis of the different spots of a coupon. The EDX analysis is used to compare the elemental ratio between electrochemically exposed and unexposed areas of the coupons.

3. Results and discussion

3.1. Accelerated corrosion test (ACT)

Considering the severity of the electrochemical degradation, the ACT protocol was adjusted for some of the coupons to avoid a complete Au-film delamination which may eliminate the possibility of the Au-film post-ACT analysis. The ACT parameters of all coupons can be found in the supporting information (section 3). The results from the ACT experiment of all Au-coated Graphite, HA and 904L coupons are shown in Fig. 2. All data from Graphite, HA and 904L coupons, are represented with grey, green and pink colour respectively throughout the paper. In the ACT data of all coupons, two distinct current profiles are observed for all coupons. The measurement starts with a sharp increase of current density with the onset of every step, followed by a transient decrease to a saturated current value. This combined feature of current profile is explained by the formation of an electrochemical double layer [15,18]. Subsequently, a saturated current density emerges as a flat plateau with time. The second characteristic feature (flat plateau) was found to be different for different coupons and also dependent on the ACT Step potential. This plateau is often termed as steady state current density and refers to the accompanying electrochemical processes. Considering the experimental parameters, the accompanying electrochemical processes can be narrowed down to two possibilities; electrochemical oxidation of the coupon and oxygen evolution reaction (except Step 1).

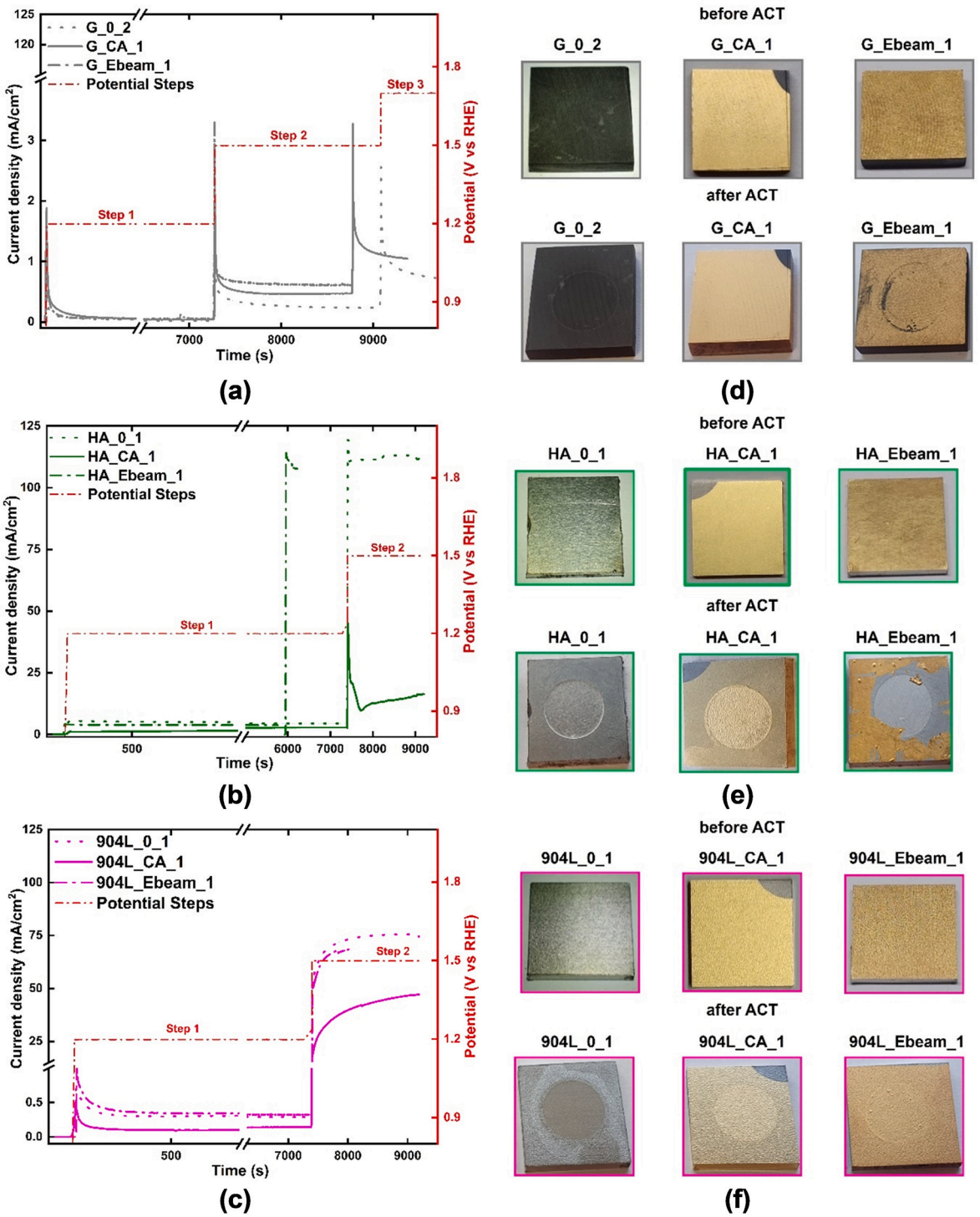

Fig. 2. Results from the ACT of different coupons with and without Au-coating and the photographs of the coupons: In figure (a), (b) and (c), the current profiles of all Graphite, all HA and all 904L coupons are shown. As a side-by-side comparison, the photographs of all Graphite (d), HA (e), and 904L (f) coupons before and after ACT are shown next to the ACT data.

For this work, the effect of oxygen evolution reaction is not further considered. So, the inherent resistance of the coupons against this electrochemical oxidation is being interpreted as their corrosion resistance under different ACT Steps i.e. within the SDE operating conditions. Hence, the coupon with the lowest steady state current density can be identified as the best performing against electrochemical corrosion with respect to corresponding ACT steps.

Fig. 2(a) shows that among the uncoated coupons, Graphite exhibits the lowest steady-state current density, HA the highest, and 904L an intermediate response. Upon Au-coating, the steady-state current density of all coupons decreases with time, except for Au-coated Graphite. Between the two PVD-based coatings, coupons with CA Au-films consistently show lower current densities than those with E-beam Au-coatings and this trend appears consistent for all three Au-coated bipolar plate materials. Time-stamped photographs were taken during ACT (SI Section 3) to reveal electrolyte colour changes associated with

corrosion. It was observed that the electrolyte remains transparent throughout the ACT of all Graphite coupons. In contrast, the electrolyte for uncoated HA turned yellow after approximately 30 min at Step 1 (1.2 V), with colour intensity increasing over time and step potential. During the run of ACT Step 2 on uncoated HA, some bubbling was observed at the surface. As discussed earlier, possibly this gas evolution took place due to oxygen evolution reaction and can also be correlated to the observed high current density (Fig. 2(b)). When HA is coated with E-beam Au-coating, the electrolyte turned yellow around 30 min at Step 1 similar to the uncoated HA. Considering this significant corrosion and attributing it to poorer protection from the E-beam Au-coating for the HA substrate underneath, the ACT protocol was shortened to conserve some Au-film. After running the experiment for 98 min at Step 1, Step 2 was initiated and was kept for 5 min only. At Step 2, substantial amount of material detachment from the coupon surface is witnessed accompanied by a deep yellow colour in the electrolyte (SI section 3). In comparison, HA coated with CA Au-coating, exhibited only faint yellow coloration after 90 min in Step 1 and light yellow after step 2. From this comparison of visual observation, it can be anticipated that CA Au-coating provides a better coating protection than E-beam Au-coating on HA and can also be concurred by their comparable current densities at both Steps. For uncoated 904L, no colour change was observed in the electrolyte during ACT Step 1 (Fig. 2(c)–SI section 3). However, leaching of corrosion product from the coupon surface was spotted as soon as the potential was raised to Step 2 accompanied by yellow colour in the electrolyte. These results reflect the comparable corrosion behaviour of the two metallic uncoated coupons within Step 1 and Step 2. When 904L is coated with E-beam Au-coating, the electrolyte remained colourless during Step 1, but the coupon surface began to give off yellow debris into the electrolyte from the start of Step 2 (SI section 3). Given the superior stability of 904L over HA, the ACT was extended for 10 min at Step 2. Taking the results of CA Au-coated HA as a reference, the ACT protocol is performed for 120 min at Step 1 and 30 min at Step 2 for CA Au-coated 904L. Here, the electrolyte appeared colourless at Step 1 leading to the presence of a faint yellow electrolyte during Step 2 (SI section 3). The current density of CA Au-coated 904L is found to be lower than E-beam Au-coated 904L in both Steps. Altogether, the overall experimental observation suggests that the intensity of electrochemical corrosion accelerates with the progression of different ACT Steps and a clear distinction of electrochemical stability and corrosion resistance can be recognized among uncoated bipolar plate materials. Uncoated Graphite is observed to be stable up to Step 3 (1.7 V), then moderately stable 904L till step 2 and HA being the least stable. This analysis imparts significant knowledge about the electrochemical stability of different bipolar plate materials under the influence of realistic SDE conditions. Considering the visual observation (SI section 3) and the ACT data, CA Au-coating demonstrates superior protective performance compared to E-beam Au-coating.

To visually examine the state of the Au-coated coupons, photographs were taken before and after ACT. These photographs can be found in Fig. 2(d), (e) and (f). Before the ACT, Au-coated coupons did not show any adherence issue or macroscopic defects. From the photos of the coupons after ACT, every coupon showed a circular mark at the centre of the surface due to the exposure to the electrolyte. Therefore, the comparison between the electrochemically exposed central area and the electrochemically unexposed peripheral area can be evaluated to see the effect of ACT. In many cases taking a clear well-focused photo was difficult such as the 904L coupons due to the surface roughness of the coupon. Therefore, for deriving appropriate scientific conclusion, SEM was performed on all the coupons which will be discussed later. In the uncoated Graphite and CA Au-coated Graphite coupon, only minor changes in surface morphology were observed after ACT. No significant damage or signs of delamination was found. On the surface of the E-beam Au-coated Graphite, circular markings were seen coming from the fastening of the coupon to the cell with the gasket. But significant surface degradation was found on both uncoated metallic coupons in the post ACT state. The mass loss in the electrochemically exposed areas of uncoated HA and 904L could be visibly identified as a result of electrochemical corrosion. From the photographs of Fig. 2(e), almost all of E-beam Au-film was detached from HA with only a small Au-fragment still adhering to the HA surface. The adherence of the E-beam Au-coating was possibly weakened during the ACT and the delaminated HA surface exhibited clear signs of roughening, further confirming electrochemical corrosion taking place beneath the detached Au-coating. This type of delamination was not encountered in any other coupons. In comparison, CA Au-coating on HA was found to be stable after ACT but some roughening was observed after ACT. On the 904L coupons, both Au-coating methods remained well adhered after the ACT. As a qualitative visual comparison, it can be distinguished that the effect of the ACT on both Au-coatings is less intense when 904L is utilized as bipolar plate coupon compared to HA. As a confirmation, the E-beam Au-coating on HA is delaminated but the same E-beam Au-coating on 904L survived the ACT. In case of CA Au-coated HA, a roughening or pitting effect is observed on the Au-film surface. On the other hand, only minor effect of the ACT is observed for CA Au-coated 904L.

3.2. *In-situ elemental analysis with ICP-OES*

To quantitatively evaluate the corrosion products during ACT, electrolyte samples were collected at the end of each ACT step and analysed using ICP-OES. The timing of electrolyte collection is shown in the Supporting Information (SI section 4). For a comparative evaluation, all the results from ICP-OES elemental analysis of all coupons from Step 1 (1.2 V) and Step 2 (1.5 V) are presented in Fig. 3. The detection threshold of ICP-OES (0.50 mg/kg) is marked by a horizontal red dashed line in all panels of Fig. 3. A control sample consisting of fresh unused electrolyte (20 wt% H_2SO_4) was analysed to establish a baseline where only a trace amount of Fe was detected (0.58 mg/kg).

In Fig. 3(a) and (b), the ICP-OES results from electrolyte analysis of the Graphite coupons can be compared. It can be seen that no elemental concentration was found above the ICP-OES detection limit for all the Graphite coupons. Only a trace amount of Fe- was found in the case of E-beam Au-coated Graphite coupon similar to the control sample. This ICP-OES data is consistent with the visual observation with no colour change of the electrolyte solution, indicating negligible electrochemical corrosion of Au-coated Graphite coupons. In Fig. 3 (c), the ICP-OES data for uncoated HA and Au-coated HA from ACT Step 1 is shown. Here, the data reveal detectable concentrations of Fe-, Ni- and Cr-in the electrolyte for all coupons. Given that HA is a Ni-based alloy, Ni-ion concentration serves as a good indicator of bipolar plate degradation. After comparing the ICP-OES data for all HA coupons at Step 1, it can be confirmed that the uncoated HA has experienced the highest electrochemical corrosion as reflected by the highest Ni-ion concentration. It is also clear that different metal concentrations in the ICP-OES data decrease when HA is coated with a protective Au-coating. From the ICP-OES data from the electrolyte samples of Step 2, the concentration of Fe-, Ni- and Cr- are found to be increasing for all HA coupons (Fig. 3 (d)). This increase of metal element concentration in electrolyte with step potential is indicative of the ongoing electrochemical corrosion and can also be correlated to the colour change of the electrolyte. From these data, it can be clearly assessed that Ni-concentration from ICP-OES is slightly higher in the case of E-beam Au-coating compared to CA Au-coating. As observed, CA Au-coated HA outperforms E-beam coated HA in reducing metal ion presence from the bipolar plates within the electrochemical conditions of Step 1 and Step 2. These findings align with the visual observation and validate the higher protective performance of CA Au-coating on HA substrates under similar electrochemical conditions. For all 904L coupons, Fe-concentration in ICP-OES data can be taken as a reference to interpret the extent of electrochemical corrosion. From Fig. 3 (e), the ICP-OES data for ACT step 1 revealed only trace amounts of Fe-from the uncoated 904L and concentrations below the detection limit for all Au-coated 904L coupons. The ICP-OES data for ACT Step 2 from all 904L

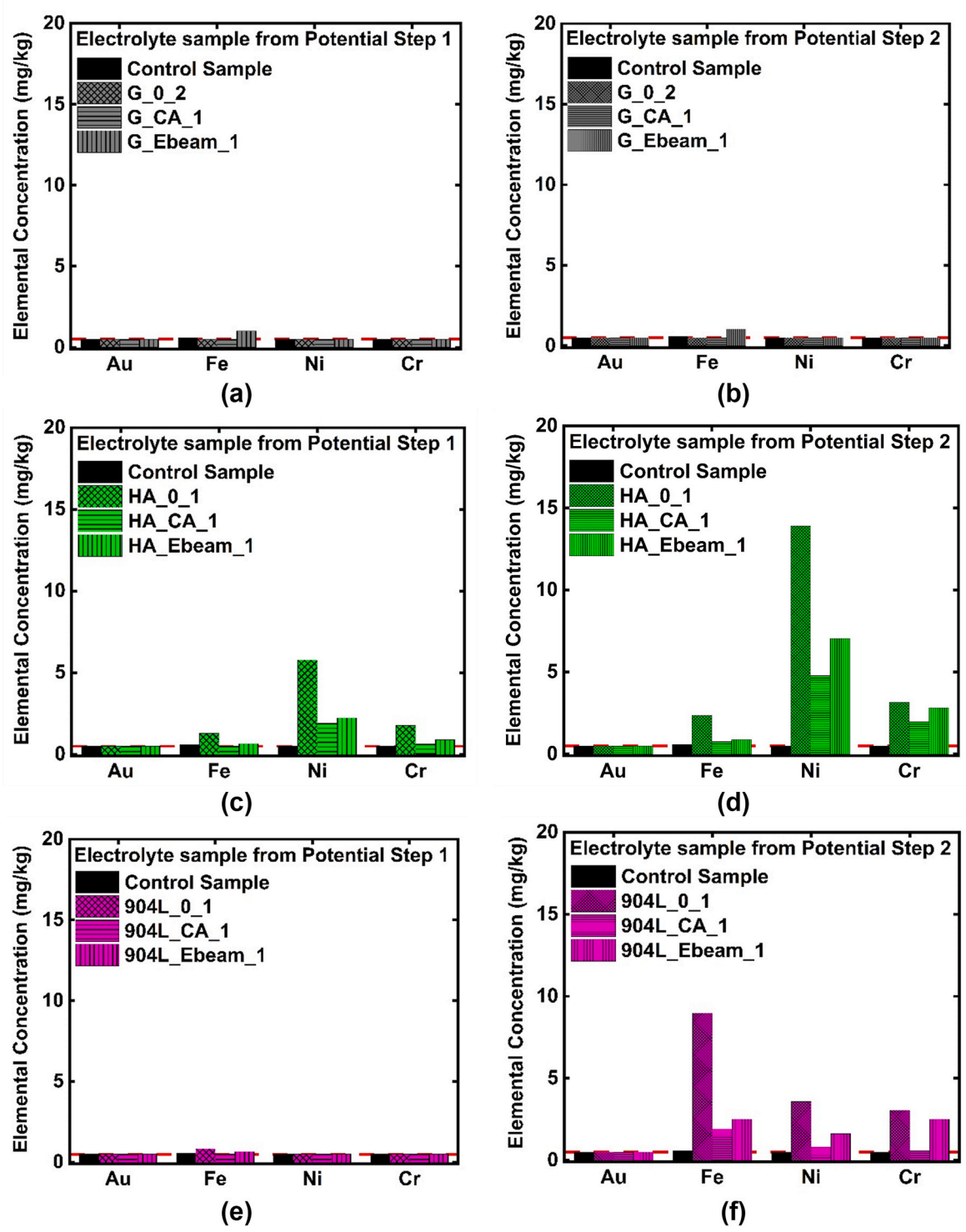

Fig. 3. ICP-OES elemental analysis data of all coupons: Here, the presented ICP-OES data is normalized to 10 ml volume. First row shows the ICP-OES data for all Graphite coupons from the electrolyte correlating Step 1 (a) and Step 2 (b). The second row shows the ICP-OES data from all HA coupons for Step 1 (c) and Step 2 (d). The last row shows ICP-OES data from all 904L coupons from Step 1 (e) and Step 2 (f). The reference composition of uncoated HA is 62% Ni, 5.13% Fe, 11.60% Cr, 12.80% Mo, 3.27% W and uncoated 904L is 47.20% Fe, 26.5% Ni, 18.10% Cr, 2.73% Mo, 0.60% Mn (measured using EDX).

coupons is shown in Fig. 3 (f). Here, different metals Fe-, Ni-, Cr- in electrolyte were detected correlating with the appearance of yellow colour in the electrolyte during Step 2. From the data, the Fe-conc. is the highest for uncoated 904L and lowers with the protective Au-coating. By comparing Fe-concentration from the CA Au-coated and E-beam Au-coated 904L plotted in Fig. 3 (f) and (d), it can be confirmed that CA Au-coating shows a higher anticorrosive performance at the electrochemical conditions of Step 2 for both metallic bipolar plate materials. The ratio of alloying elements; Fe-, Ni- and Cr- is consistent among different coupons of HA and 904L supporting the reliability of the measured ICP-OES data.

Considering all ICP-OES data, a clear trend in corrosion resistance emerges under the dynamic conditions of different ACT steps. The uncoated 904L displays a good corrosion resistance consistently with or

without Au-coating in the electrochemical conditions of Step 1 showing minimal to no detectable corrosion products (Au-, Fe-, Ni- and Cr-) followed by a moderate performance in the electrochemical conditions of Step 2. In contrast, uncoated Hastelloy showed the least corrosion resistance with severe degradation even at the mild potential of Step 1 and further in Step 2. Graphite coupons demonstrated the best corrosion resistance consistently throughout all the steps. Among the Au-coated metallic coupons, the data from two sets of E-beam Au-coated coupons suggest that it is unable to offer effective corrosion protection as indicated by elevated metal ion concentrations in the electrolyte. In contrast, the CA Au-coating consistently delivered superior protection than E-beam Au-coating irrespective of bipolar plate materials, as reflected in their significantly low levels of metal concentrations in electrolyte. On Graphite substrates, both coatings were able to provide adequate corrosion protection and can be nominated as a suitable method for protective Au-coatings. These outcomes can be further confirmed by examining the photographs from visual observation (SI section 3).

3.3. Electrochemical corrosion metric 1

Since the material loss from all coupons were solely driven by the electrochemical corrosion imposed by ACT parameters in 20 wt% H_2SO_4, the ratio of total metallic concentrations in electrolyte from Au-coated and uncoated bipolar plate materials represents the dynamic corrosion resistance of that particular Au-coating for that bipolar plate material. This metric can be defined as the Corrosion Protection Efficiency (CPE) which is a function of applied corrosion potential, duration, electrolyte and Au-coating method. The mathematical expression for CPE is represented in Eq. (2) below.

$$\text{Coating Protection Efficiency } (\%) = [1 - (M_{coated} / M^{\circ}_{uncoated})] \times 100\% \quad \text{Eq. 2}$$

where $M^{\circ}_{uncoated}$ and M_{coated} represent the total metal ion concentrations (Fe-, Ni-, Cr-) in the electrolyte of equivalent volume from uncoated and coated coupons. This metric provides a normalized assessment of how well a coating mitigates bipolar plate degradation under dynamic electrochemical condition. This approach allows for a direct, experimental data driven comparison between different coating methods and bipolar plate materials. The calculated CPE of the two different Au-coating methods is compared in Fig. 4. From Fig. 4, the CPE data is close to

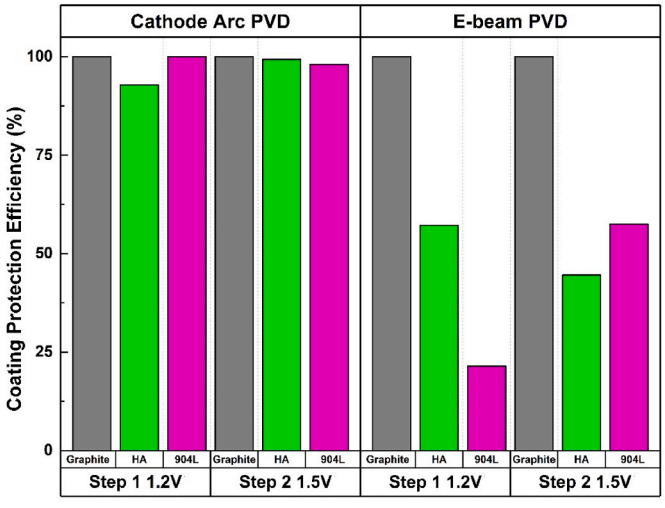

Fig. 4. Electrochemical corrosion metric 1: the calculated CPE for different Au-coating methods according Eq. (2) to is shown here. The data is shown here with regards to their substrate and electrochemical condition of ACT Step 1 and Step 2.

100% for nearly all CA Au-coated bipolar plate materials within the electrochemical conditions of ACT Step 1 and Step 2. The deviation of CPE of HA_CA_1 coupon at Step 1 can be explained by the volumetric normalization of ICP-OES data as higher volume of electrolyte was utilized in case of Step 2 compared to Step 1 (SI section 4). Conversely, the CPE value drastically decreased for HA and 904L coupons when they were coated with E-beam Au-coating in the equivalent electrochemical conditions. Taking reference of the current profile in ACT (Fig. 2) and ICP-OES data (Fig. 3) a clear trend is observed for E-beam Au-coated HA that upon transitioning from Step 1 to Step 2 involved significant metallic dissolution in the electrolyte. There is a decrease of CPE from 57% to 44% from Step 1 to Step 2 for E-beam Au-coated HA. In principle, the similar trend should have developed for E-beam Au-coated 904L regarding the ascending corrosion potential from Step 1 to Step 2 but this is not observed. CPE is mainly controlled by the ratio of $M_{coated}/M^{\circ}_{uncoated}$ and this discrepancy comes from Step 1 ICP-OES data of 904L_Ebeam_1. The E-beam Au-coated 904L coupon showed an Fe-conc. of 0.65 mg/kg in the Step 1 electrolyte. Since the magnitude of this discrepancy is rather small (Fe-conc. = 0.65 mg/kg) and similar result was also found in the control sample (Fe-conc. = 0.58 mg/kg), it can be considered as an artifact. This artifact originates from the necessary electrolyte sample processing before ICP-OES measurement. Further investigation of this discrepancy is limited by the detection ability of ICP-OES (0.50 mg/kg). In conclusion, according to the electrochemical corrosion metric 1, CA Au-coating exhibits higher CPE than E-beam Au-coating within the electrochemical condition of Step 1 and Step 2 which is in full agreement with the previously presented data.

3.4. Estimation of corrosion rates

The I_{corr} measurement was performed before and after the ACT of all coupons to calculate their Corrosion Rates (CR) (Fig. 5). From the I_{corr} measurement data of Fig. 5, the Linear Polarization Resistance (R_p) was calculated first. The Stern-Geary equation (Eq. (3)) relates R_p and Tafel constants (β_a, β_c) to evaluate the corresponding I_{corr} [19]. The I_{corr} value is used in the mathematical interpretation of Faradays' law to calculate the Mass loss (Eq. (4)) and Corrosion rate (Eq. (5)) using the following equations:

$$\text{Corrosion Current, } I_{corr} = \frac{1}{2.303} \frac{\beta a.|\beta c|}{(\beta a + |\beta c|)} \frac{1}{Rp} \quad \text{Eq. 3}$$

$$\text{Mass loss} = \frac{M.W}{n\,F} I_{corr} \quad \text{Eq. 4}$$

$$\text{Corrosion rate} \Big/ \text{Penetration depth} = \frac{M.W}{n\,F\,A\,\rho} I_{corr} \quad \text{Eq. 5}$$

where; I_{corr} = corrosion current (μA), M.W = Molecular Weight (g/mol), n = valency, F = faradaic charge (96,485 C/mol), A = geometric area (cm^2), ρ = density (g/cm^3), β_a, β_c are anodic and cathodic slopes (mV/decade), R_p is the Linear Polarization Resistance (Ω). The calculated mass loss rate and CR can be found in section 5 of the supporting information. The calculated mass loss rate and CR values of uncoated 904L and HA are found to be comparable with reported values in literature [9, 20].

3.5. Electrochemical corrosion metric 2

The CR shifts of all the Au-coated coupons are presented along with their respective mean values in Fig. 6. In all Au-coated coupons, the calculated CR was observed to shift from low to higher values due to the ACT. As discussed earlier, the ACT protocol is designed to cause electrochemical corrosion on the Au-coated bipolar plates, therefore, the observed shift in CR from before to after ACT can be interpreted as an indicator for the long-term electrochemical stability of the coupons, termed as the second electrochemical corrosion metric. From Fig. 6, the

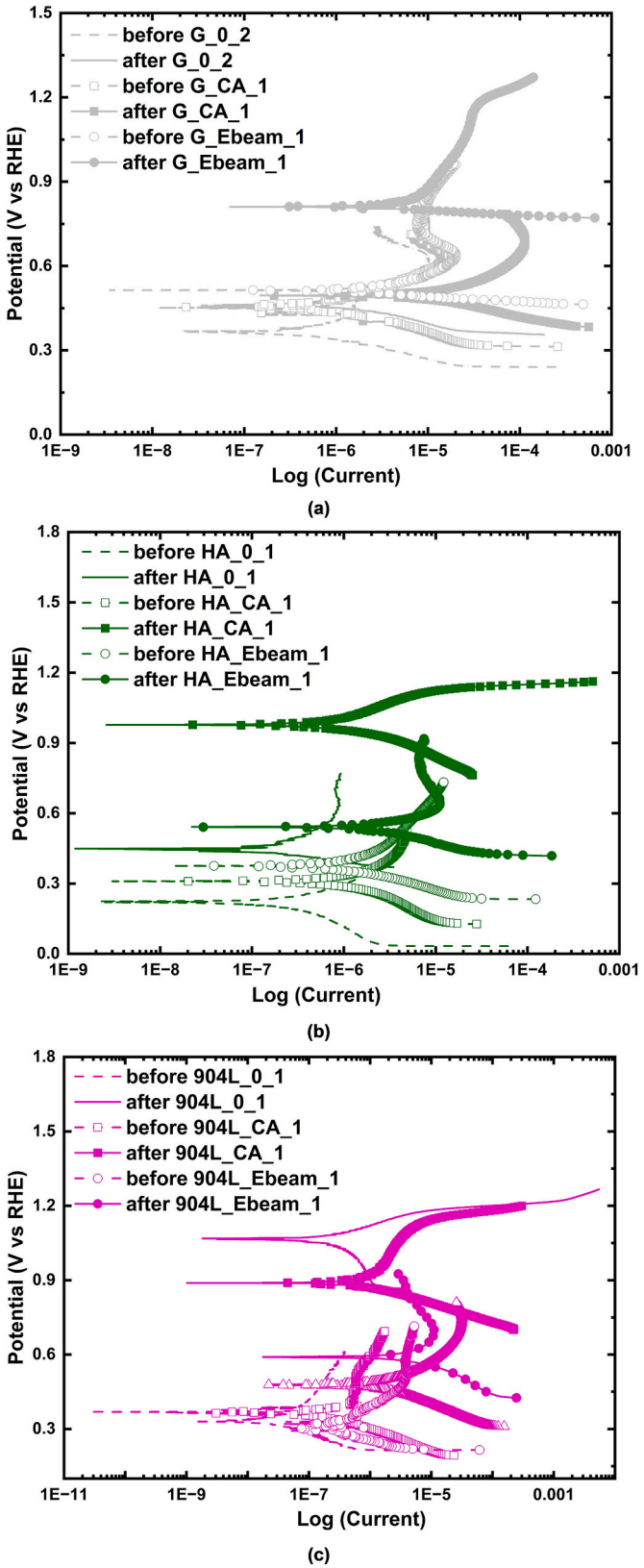

Fig. 5. I_{corr} measurements of the coupons: (a) all Graphite coupons, (b) all HA coupons and (c) all 904L coupons. After ACT, it can be identified that the current-voltage polarization curves shift to higher current density for all the coupons. This reflects the increase of corrosion in all the coupons. For the metallic coupons, the OCP was found to increase after ACT which can be correlated with passivation characteristics.

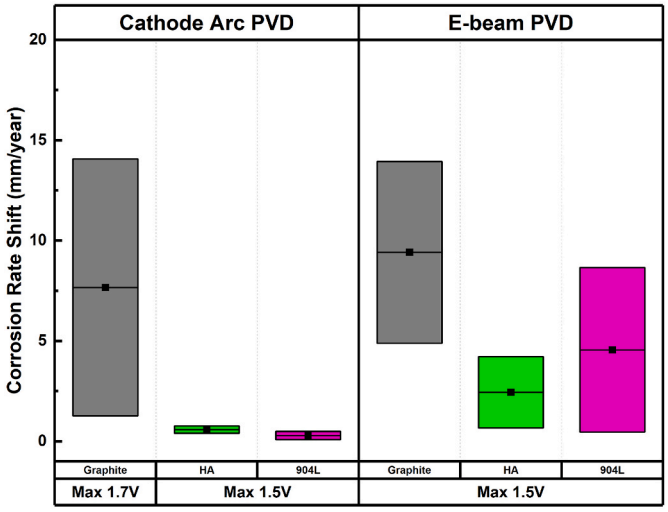

Fig. 6. Corrosion Rate shifts of all coupons: The data is represented with the corresponding Au-coating method, Substrate and their corrosion potential during ACT.

observed CR shifts for CA Au-coated HA and 904L coupons are found to be 0.40 to 0.76 and 0.08 to 0.49 mm/year. Considering the ACT protocol, both CA Au-coated HA and 904L experienced a maximum potential of 1.5 V for 30 min. In contrast, CA Au-coated Graphite exhibited a significantly larger CR shift which can be correlated to the higher corrosion potential (Step 3- 1.7 V) during its ACT. In the case of E-beam Au-coated HA and 904L, both coupons show larger CR shifts compared to CA Au-coated coupons, despite undergoing a shorter ACT run (SI section 2). Therefore, the minimal CR shift indicates that the CA Au-coating is capable of offering a better long term electrochemical stability for metallic bipolar plates within the combined potential range of Step 1 and Step 2.

Similar to CA Au-coated Graphite, the E-beam Au-coated Graphite also showed larger CR shift compared to E-beam Au-coated HA and 904L coupons. This higher CR shift of E-beam Au-coated Graphite can be explained by a longer ACT protocol (SI section 2) compared to the metallic bipolar plates. The CR shifts of different Au-coated Graphite coupons indicate a common phenomenon. From Fig. 6, it can be identified that after the ACT, E-beam Au-coated Graphite reaches a similar CR like CA Au-coated Graphite even though a shorter ACT protocol with lower corrosion potential was applied on it. CA Au-coated Graphite was subjected to a higher corrosion potential of 1.7 V and E-beam Au-coated Graphite experienced up to 1.5 V. Therefore, it can be confirmed that the long-term electrochemical stability of CA Au-coated Graphite is higher than E-beam Au-coated Graphite. In addition to this, a common tendency was observed that Graphitic coupons showed higher CR shifts than metallic bipolar plates. It can be proposed that this particular difference of CR shifts stems from the existence of passivation layer of the metallic bipolar plate materials only [21,22]. Overall, the superior corrosion resistance of the CA Au-coating was evident on both metallic coupons with significantly smaller CR shifts and this distinction became even clearer when the CR shifts of Au-coated Graphite coupons are compared.

3.6. Morphological investigation with Scanning Electron Microscopy

The central electrochemically exposed area and the peripheral electrochemically unexposed pristine area of the coupons were considered for a comparative HR-SEM image analysis (Fig. 2(d), (e), (f)). The SEM images from different uncoated coupons are presented in Fig. 7. In the low magnification SEM image of Fig. 7 (a), the boundary between the electrochemically exposed and unexposed area of uncoated Graphite

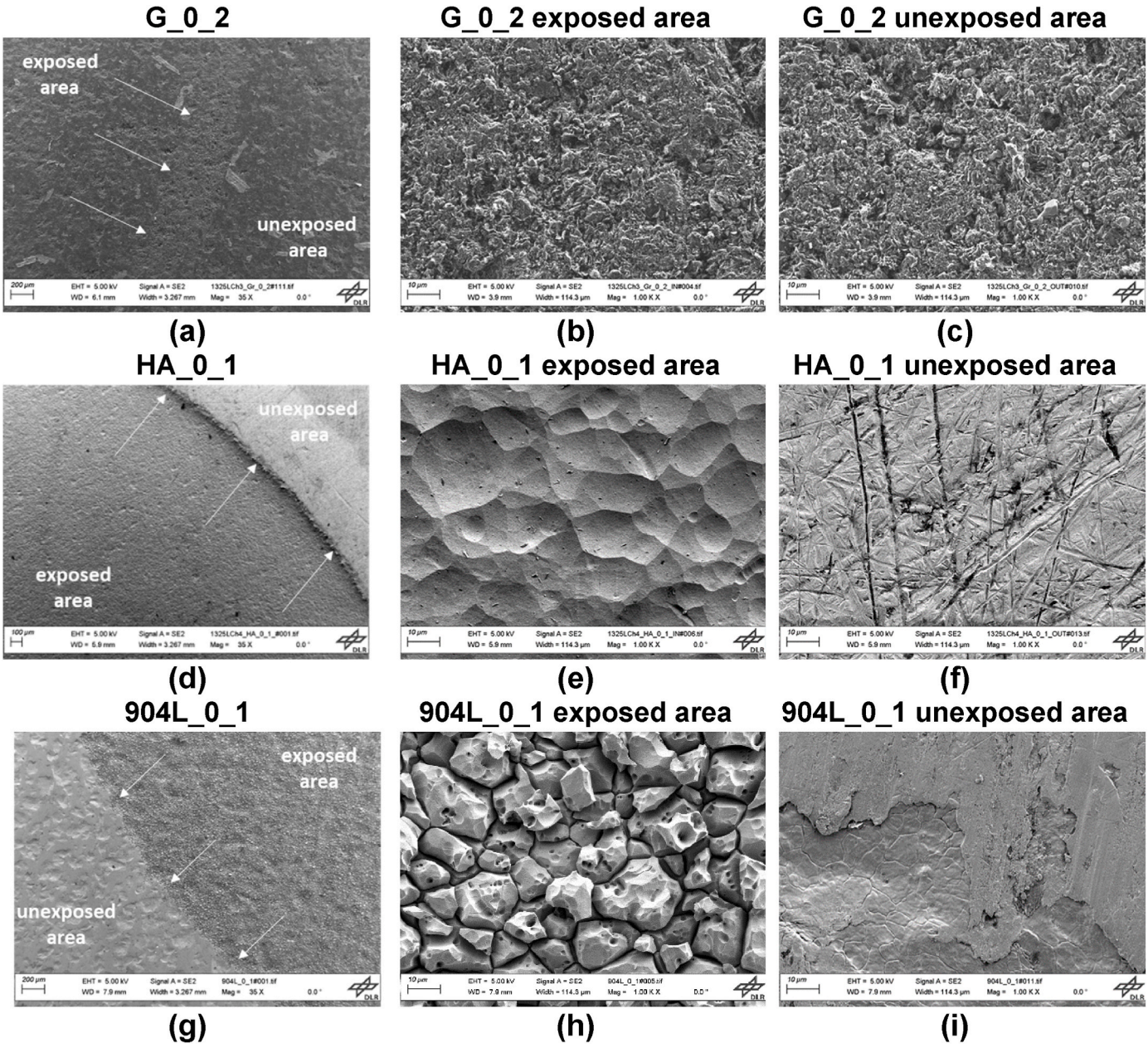

Fig. 7. SEM images of the uncoated coupons: In the low magnification SEM images of uncoated Graphite, HA and 904L can be found in figure (a), (d) and (g). The three white arrows indicate the boundary line between the electrochemically exposed and unexposed area. The HR-SEM images from electrochemically exposed and unexposed area of uncoated Graphite are shown in (b) and (c). Similarly, images from different areas of uncoated HA are shown in shown (e) and (f). Lastly, the images from different areas of uncoated 904L are shown in (h) and (i).

is highlighted with three white arrows. The arrows were drawn from the exposed area towards unexposed area. The HR-SEM images taken from the electrochemically exposed and unexposed surface of Graphite can be seen in Fig. 7(b) and (c). In both images, the Graphite surface morphology appears to be similar, with more flat features on the unexposed surface compared to the exposed surface. This change can be understood as an effect of the ACT on Graphite surface. In Fig. 7 (d) and (g), the boundary between electrochemically exposed and unexposed area of uncoated HA and 904L coupon can be clearly pinpointed with white arrows. In both images, the mass loss from the uncoated coupon surface is evident and appears to be more intense for uncoated HA than uncoated 904L as a clear step edge can be identified at the boundary. The HR-SEM images of uncoated HA and 904L from Fig. 7 (e) and (h) revealed that their electrochemically exposed surface was significantly corroded by ACT. The pristine polished flat surface of HA (Fig. 7 (f)) became rough with wavy patterns as a result of electrochemical corrosion (Fig. 7 (e)). In case of the uncoated 904L, the pristine morphology of uncoated 904L (Fig. 7 (h)) transforms into an irregular particle shaped structure with deep trenches (Fig. 7 (i)). This major structural change of uncoated 904L can be validated as the consequence of electrochemical corrosion from ACT. In Fig. 8, HR-SEM images from the electrochemically exposed areas of CA Au-coated and E-beam Au-coated coupons are shown. The images from the unexposed area of the corresponding Au-coated coupons can be found in section 6 of supporting information. From the HR-SEM images of all three CA Au-coated coupons in Fig. 8(a)–(c) and (e), it becomes evident that the CA Au-coating shows a uniform morphology on all three bipolar plate materials. On the other hand, HR-SEM images captured from the electrochemically exposed areas of E-beam Au-coated Graphite (Fig. 8 (b)), HA (Fig. 8(d)) and 904L (Fig. 8(f)) exhibits different morphologies. On Graphite, E-beam Au-coating shows

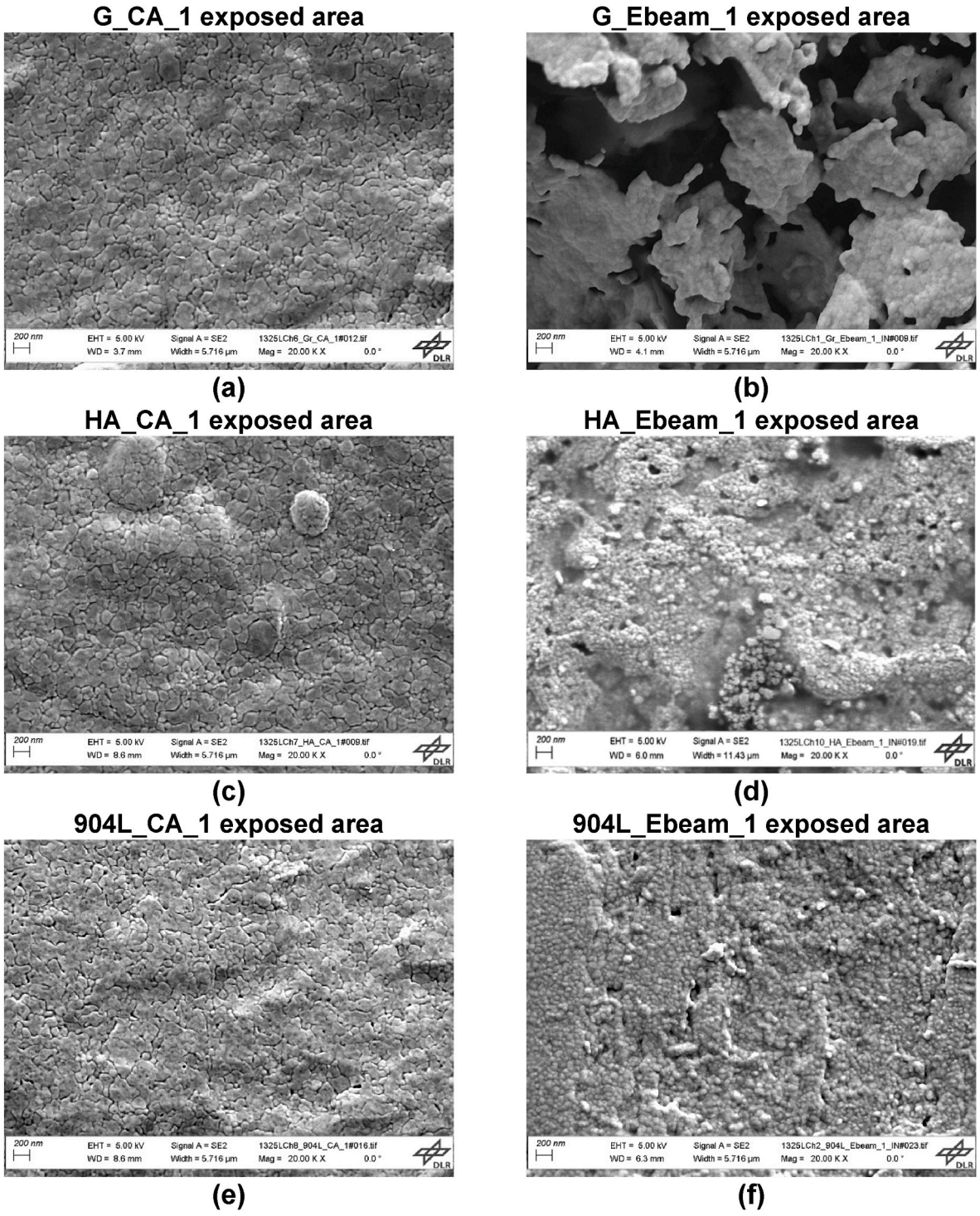

Fig. 8. HR-SEM analysis of the electrochemically exposed areas of all Au-coated coupons: HR-SEM images in the left column are taken from the electrochemically exposed area of CA Au-coated Graphite (a), HA (c) and 904L (e). In the right column, HR-SEM images from the electrochemically exposed area of E-beam Au-coated Graphite (b), HA (d) and 904L (f) are organized.

a porous morphology which is considered undesirable from a coating protection aspect. For HR-SEM imaging of E-beam Au-coated HA (Fig. 8 (d)), the remaining small Au- fragment after delamination was considered which revealed a rough morphology with the formation of ridges and pinhole like pockets. These unwanted features can be correlated with inhomogeneous film formation. From Fig. 8(f), the coverage of E-beam Au-coating on 904L coupon appeared more homogenous than HA but still step-edge formation and voids are observed. Considering HA and 904L, the inhomogeneity of E-beam deposited Au-coating and existence of pores allows the electrolyte to reach and interact with the underlying substrate facilitating the electrochemical corrosion of the substrates. It can be proposed that the similar mechanism of corrosion also takes place in case of a more homogenous and uniform CA Au-coating, but to a lesser extent. This analysis indicates that the presence of pinholes and lack of uniformity of the Au-film, as is the case for the E-beam coating, results in extreme corrosion at the Au coating/coupon interface during the ACT. This can be proposed as the failure mechanism of E-beam Au-film on the Hastelloy coupon. Still, a similar

degradation was not encountered when Hastelloy was coated with a uniform defect free CA Au-coating. The *in-situ* measured metal ion concentration data from ICP-OES analysis also concurs that the homogenous CA Au-coating is capable of protecting the bipolar plate from corrosion compared to E-beam Au-coating. The excessive metal ions observed in ICP-OES data as well as the coloration of the electrolyte from E-beam Au-coated HA correlates to the subsequent Au-film delamination. These experimental indicators can be considered as a preliminary measure for bipolar plate corrosion in SDE relevant operation. From the above-mentioned analysis, it can be concluded that CA Au-coating is capable of producing a uniform morphology across all three bipolar plates, whereas the morphology obtained from E-beam Au-coating is not suitable for the same application. The additional area-based statistical composition analysis using EDX can be found in section 7 of supporting information.

4. Conclusions

The analysis of the experimental data indicates that the CA Au coating provides the most effective protection for the bipolar plates, exhibiting the highest performance under dynamic SDE operating potentials (metric 1) and the least variation in corrosion rates (metric 2). To further validate the poor performance of E-beam Au-coating, the delaminated HA surface (previously coated by E-beam Au-coating) was analysed with SEM. It's morphology resembled the corroded surface of electrochemically exposed uncoated HA (SI Section 6). This confirms that uniform morphology of Au-coating is a crucial factor for controlling and reducing electrochemical corrosion of bipolar plate materials in the SDE application.

The experimental work and data analysis can be summarized in the following three perspectives. Firstly, the accelerated corrosion test combined with *in-situ* quantification of corrosion products provides a methodological guideline for evaluating dynamic electrochemical corrosion of Au-coated bipolar plates. Secondly, the two derived electrochemical corrosion metrics offer a comparative basis for rating corrosion resistance under SDE-relevant electrochemical conditions. Lastly, applying this methodology to two PVD-based Au-coating techniques identifies that the cathode-arc–assisted Au-coating is the superior option than electron beam evaporated Au-film. Its enhanced corrosion protection is attributed to it's higher coating uniformity and it's ability to maintain this uniformity across different bipolar-plate materials.

CRediT authorship contribution statement

Sakeb Choudhury: Writing – original draft, Visualization, Validation, Software, Methodology, Investigation, Formal analysis, Data curation, Conceptualization. **Dimitrios Dimitrakis:** Writing – review & editing, Validation, Supervision, Resources, Project administration, Methodology, Funding acquisition, Conceptualization. **Dennis Thomey:** Writing – review & editing, Funding acquisition. **Timo Ott:** Writing – review & editing, Supervision, Resources. **Céline Réthoré:** Writing – review & editing, Investigation. **Jonas Michels:** Writing – review & editing, Supervision, Resources. **Martin Kürten:** Supervision, Resources.

Declaration of competing interest

The authors declare that they have no known competing financial interests or personal relationships that could have appeared to influence the work reported in this paper.

Acknowledgements

The authors thank the European Commission for co-funding the EU Horizon project HySelect under the Grant Agreement Nr. 101101498, supported by the Clean Hydrogen Partnership and its members Hydrogen Europe and Hydrogen Europe Research. The authors would like to thank Liudmila Chernova for her supportive SEM work from "Institut für Frontier Materials auf der Erde und im Weltraum" from DLR, Köln Porz, Germany and Sarah Arnt from the F&E lab team of GRILLO Chemicals GmbH for her valuable lab assistance.

Appendix A. Supplementary data

Supplementary data to this article can be found online at https://doi.org/10.1016/j.ijhydene.2026.154628.

References

[1] Glenk G, Holler P, Reichelstein S. Advances in power-to-gas technologies: cost and conversion efficiency. Energy Environ Sci 2023;16:6058–70. https://doi.org/10.1039/D3EE01208E.
[2] Koponen J, Kosonen A, Huoman K, Ahola J, Ahonen T, Ruuskanen V. Specific energy consumption of PEM water electrolysers in atmospheric and pressurised conditions. In: IEEE conf. on power electronics and applications; 2016. https://doi.org/10.1109/EPE.2016.7695576. Karlsruhe, Germany.
[3] Franco Alessandro, Giovannini Caterina. Recent and future advances in water electrolysis for green hydrogen generation: critical analysis and perspectives. Sustainability 2023;15:16917. https://doi.org/10.3390/su152416917.
[4] Brecher LE, Wu CK. US patent US3888750A. https://patents.google.com/patent/US3888750A/en; 1974.
[5] Sattler C, Roeb M, Agrafiotis C, Thomey D. Solar hydrogen production via sulphur based thermochemical water-splitting. Sol Energy 2017;156:30–47. https://doi.org/10.1016/j.solener.2017.05.060.
[6] Wong B, Thomey D, Brown L, Roeb M, Buckingham R, Sattler C. Sulfur based thermochemical energy storage for concentrated solar power. In: ASME int. Conf. on energy sustainability; 2013. https://doi.org/10.1115/ES2013-18283. MN, USA.
[7] Brecher LE, Sprewock S, Warde CJ. The Westinghouse Sulfur Cycle for the thermochemical decomposition of water. Int J Hydrogen Energy 1977;2:7–15. https://doi.org/10.1016/0360-3199(77)90061-1.
[8] Santasalo-Aarnio A, Lokkiluoto A, Virtanen J, Gasik MM. Performance of electrocatalytic gold coating on bipolar plates for SO_2 depolarized electrolyser. J Power Sources 2016;306:1–7. https://doi.org/10.1016/j.jpowsour.2015.11.104.
[9] Outokumpu, Utilizing corrosion testing for reliable materials selection, Page-37. https://www.outokumpu.com/expertise/2020/utilizing-corrosion-testing-for-reliable-materials-selection.
[10] Nickel Institute: Alloy selection for service in Sulphuric acid, Page-6. https://nickelinstitute.org/media/4122/alloy-selection-for-service-in-sulphuric-acid-10057.pdf.
[11] Gasik MM, Virtanen J, Santasalo-Aarnio A. Improved operation of SO_2 depolarized electrolyser stack for H_2 production at ambient conditions. Int J Hydrogen Energy 2017;42:13407–14. https://doi.org/10.1016/j.ijhydene.2017.03.003.
[12] Xie L, Tian R, Xiao P, Wang L, Li Y, Qu Y, Zhang P, Chen S. Preparation of three-dimensional anodes for SO_2 depolarized electrolyzers by growing Pt clusters on graphite felt fibers. Mater Sci Eng B 2025;314:118004. https://doi.org/10.1016/j.mseb.2025.118004.
[13] Xie L, Zhang P, Tian R, Xiao P, Wang L, Chen S. Research progress in SO_2 depolarized electrolysis at INET,". Renew Energy 2025;242:122424. https://doi.org/10.1016/j.renene.2025.122424.
[14] Benck JD, Pinaud BA, Gorlin Y, Jaramillo TF. Substrate selection for fundamental studies of electrocatalysts and photoelectrodes: inert potential windows in acidic, neutral, and basic electrolyte. PLoS One 2014;9:e107942. https://doi.org/10.1371/journal.pone.0107942.
[15] Choudhury SH, Ding Y, Yi Y, Rohner C, Frandsen W, Lunkenbein T, Greiner M, Schlögl R, Heumann S. Oxidation behavior of glassy carbon in acidic electrolyte. Chemelectrochem 2022;9:e202200637. https://doi.org/10.1002/celc.202200637.
[16] Gao X, Chen J, Xu R, Zhen Z, Zeng X, Chen X, Cui L. Research progress and prospect of the materials of bipolar plates for proton exchange membrane fuel cells (PEMFCs). Int J Hydrogen Energy 2024;50:711–43. https://doi.org/10.1016/j.ijhydene.2023.09.005.
[17] Abbott WM, Murray CP, Lochlainn SN, Bello F, Zhong C, Smith C, McCarthy EK, Downing C, Daly D, Petford-Long AK, McGuinness C, Chunin II, Donegan JF, McCloskey D. Comparison of Metal Adhesion Layers for Au Films in Thermoplasmonic Applications. Applied Materials and Interfaces 2020;12:13503–9. https://doi.org/10.1021/acsami.9b22279.
[18] Yi Y, Tornow J, Willinger E, Willinger MG, Ranjan C, Schlögl R. Electrochemical degradation of multiwall carbon nanotubes at high anodic potential for oxygen evolution in acidic media. Chemelectrochem 2015;2:1929–37. https://doi.org/10.1002/celc.201500268.
[19] Angst U, Buechler M. On the applicability of the stern–geary relationship to determine instantaneous corrosion rates in macro-cell corrosion. Mater Corros 2015;66:1017–28. https://doi.org/10.1002/maco.201407997.
[20] Rashed GM, Mohrez WA, EL-Hamid AMA, Ghayad IM. Corrosion behavior of super austenitic stainless steel 904L weldment in sulfuric acid media used for leaching

application. Key Eng Mater 2019;835:384–91. https://doi.org/10.4028/www.scientific.net/KEM.835.384.
[21] Zheng C, Liu Z, Liu Q, Kong Y, Guo S, Liu C. Electrochemical behavior and passive film properties of hastelloy C22 alloy, laser-cladding C22 coating, and Ti–6Al–4V alloy in Sulfuric acid dew-point corrosion environment. Metals 2022;12:683. https://doi.org/10.3390/met12040683.
[22] Yang D, Huang Y, Peng P, Liu X, Zhang B. Passivation behavior and corrosion resistance of 904L austenitic stainless steels in static seawater. Int J Electrochem Sci 2019;14:6133–46. https://doi.org/10.20964/2019.07.14.